Journal Pre-proofs

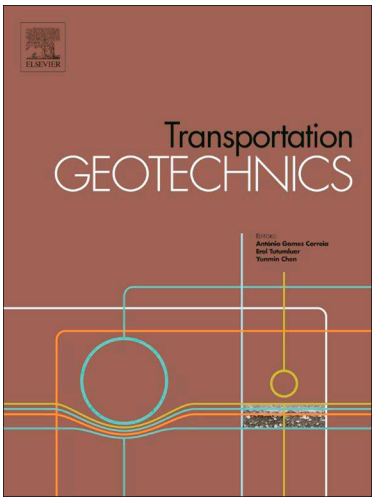


Original Article

# 3D-printed geocells in footing systems: a comprehensive physical and numerical studies on scaling and performance under centric and eccentric loading scenarios

Sarper Demirdö ğen, Ayhan Gürbüz, Kaan Yünkül

PII: S2214-3912(24)00035-7
DOI: https://doi.org/10.1016/j.trgeo.2024.101214
Reference: TRGEO 101214

To appear in: *Transportation Geotechnics*

Received Date: 5 October 2023
Revised Date: 28 November 2023
Accepted Date: 13 February 2024

Please cite this article as: S. Demirdö ğen, A. Gürbüz, K. Yünkül, 3D-printed geocells in footing systems: a comprehensive physical and numerical studies on scaling and performance under centric and eccentric loading scenarios, *Transportation Geotechnics* (2024), doi: https://doi.org/10.1016/j.trgeo.2024.101214

This is a PDF file of an article that has undergone enhancements after acceptance, such as the addition of a cover page and metadata, and formatting for readability, but it is not yet the definitive version of record. This version will undergo additional copyediting, typesetting and review before it is published in its final form, but we are providing this version to give early visibility of the article. Please note that, during the production process, errors may be discovered which could affect the content, and all legal disclaimers that apply to the journal pertain.

© 2024 Published by Elsevier Ltd.

# 3D-printed geocells in footing systems: a comprehensive physical and numerical studies on scaling and performance under centric and eccentric loading scenarios.

**Sarper Demirdöğen, Ayhan Gürbüz*, Kaan Yünkül**

*Gazi University, Faculty of Engineering, Department of Civil Engineering, 06570, Ankara, Turkey*

*****Corresponding author.

*E-mail address:* agurbuz@gazi.edu.tr (A. Gürbüz), sarper.demirdogen@gazi.edu.tr (S. Demirdöğen), kaanyunkul@gazi.edu.tr (K. Yünkül).

## Abstract

The complexities of scaling have long presented challenges in applying small-scale test results of geocell-reinforced footings to field conditions in geosynthetic engineering. There has been no research that thoroughly examines the scaling of both geometry and material stiffness in geocell-reinforced footing systems although limited studies have attempted to scale geocells using alternative materials with lower strength, such as simile paper, non-woven geotextile etc. Therefore, this is a leading study to address the complexities of scaling using 3D-printing technology, where both geometry and tensile stiffness of geocell were accurately scaled using scaling laws. In the present study, the impact of scaling on the performance of strip footings reinforced with both traditional fabricated and 3D-printed geocells in terms of pressure-settlement response and improvement factors were assessed. The results indicated that 3D-printed geocells offered significant advantages in customization and rapid prototyping of field scale. Specifically, the strip footings reinforced with fabricated geocells showed up to 65% higher improvement factors in both loose and dense soils compared to those using the scaled 3D-printed geocells. Furthermore, the footings reinforced with scaled geocells using 3D-printing technologies closely aligned with existing large-scale test results regarding improvement factors, which were further validated through various numerical analyses. These findings offer new perspectives for optimizing and applying 3D-printed geocells in geotechnical engineering and address the longstanding challenge of scaling geocell-reinforcement systems in small-scale model tests.

**Keywords:** Geocell-reinforced footings, 3D-printed geocells, Strip footings, Centric and eccentric loading, PLAXIS 3D, Scale effect

## 1. Introduction

The role of geocells in enhancing soil structures has emerged as a crucial topic in sustainable construction and advanced infrastructure development. The geocell, a honeycomb structure,

effectively improves the mechanical properties of soils, which leads to an increase in the bearing capacity of the footings and a reduction in their settlements. This enhancement is achieved by confining the lateral movement of the soil particles, distributing the footing pressure over a larger area and increasing friction between soil particles and the geocell wall surface. The challenge of scaling, specifically on the imprecise extrapolation of results from laboratory model tests to prototype or large-scale field applications, remains a major obstacle to fully understanding the behavior and improvement effects of geocell reinforced footing systems despite these advantages of geocells [1].

In geocell-reinforced footing systems, small-scale laboratory tests are generally favored over large-scale modeling due to their ability to facilitate rapid testing and parametric studies, thereby identifying key factors that influence the behavior of the systems. However, the results obtained from the laboratory model tests may differ from those gathered in large-scale experiments due to the scale effect [2-10]. Dimensional analysis, which is based on scale law and used for small-scale models, is preferred to predict the performance of the prototype geosynthetic reinforced footing in field conditions [11-20]. However, a limitation arises when using conventional commercial geocells in the experimental studies. Due to performed dimensional analysis, these geocells can inadvertently represent materials with exceptionally high tensile strength that are not available in practical field applications.

Scaling down the geometrical dimensions of each constituent element is essential when conducting model tests. However, according to established similarity law, merely adjusting the dimensions is not sufficient; it is equally important to modify the material properties, such as tensile strength and stiffness [6-8,13,14,21]. Recent research and guidelines on geocells highlight that the properties of raw material and geometry strongly influence their reinforcement effectiveness [1,22,23]. Correspondingly, key material parameters include elastic stiffness and resistance to permanent deformation [1]. Therefore, scaling both the material properties and geometry should be considered when investigating geocell-reinforced systems in model tests. Although several studies have attempted to scale geocells using alternative materials with lower strength, such as simile paper, India paper, non-woven geotextile etc. [24,25], there has been no research that thoroughly examines both geometry and material modulus in geocell-reinforced footing systems.

The emergence of 3D-printing in the mid-1980s marked a groundbreaking technological revolution. The advent of 3D-printing technology has significantly impacted geotechnical engineering by enabling the fast development and customization of geosynthetic materials. Recently, 3D-printing has also been adopted in geosynthetic research for simulating prototype behavior. Stathas et al. [26] investigated to preparation of model geogrids with properly scaled geometry and tensile behavior for small-scale laboratory tests. Arab et al. [27] explored the impact of various parameters on improvement factors using bio-inspired 3D-printed honeycomb geogrids in model tests. Their study optimized the geogrid design, achieving significant enhancements in the bearing capacity of the soil under examination. Research by Zhang et al. [28] demonstrated the innovative use of fiber Bragg grating (*FBG*) 3D-printed geogrids for both reinforcement and deformation monitoring in road subgrades over karst caves, offering valuable insights for tackling complex geotechnical challenges in road construction within karst regions. Zeng et al. [29] investigated the cyclic shear interaction of coarse-grained soil with 3D-printed stereoscopic geogrid material. They observed that 3D-printed stereoscopic geogrid significantly improves the cyclic shear interface strength of coarse-grained soil than traditional commercial planar geogrid. However, to the best of the author's knowledge, limited studies have been conducted on the application of 3D-printed geocells for scaling purposes.

The primary objective of this study is to address the challenge of scaling in the context of reinforced strip footings with 3D-printed geocells. To achieve this, scaled geocell models were first produced using 3D-printing technology, where both geometry and model tensile stiffness were accurately scaled using scaling laws. Subsequently, small-scale tests were conducted to assess the performance of footings reinforced with traditional fabricated and 3D-printed geocells, focusing especially on footing pressure-settlement characteristics and improvement factors. Three dimensional numerical analyses were also performed to validate the small-scale experimental results and simulate corresponding large-scale or prototype scenarios. This approach broadens the scope of this study from precisely scaled laboratory tests to exploring the potential implications of these models in field conditions, considering unexpected influential parameters. This research is expected to advance the geocell field by scaling geocell materials, allowing model experiments to represent in field applications more accurately.

## 2. Dimensionless analysis and scale factor

Small-scale laboratory tests are generally preferred over large-scale modeling because they allow numerous tests to be conducted quickly and facilitate parametric studies identifying the key factors affecting behavior [6]. However, the scaled model test results may differ from those gathered in large-scale experiments due to the scale effect. In small-scale models, dimensional analysis and scale law can be thoroughly examined to mitigate the scale effect and to predict the performance of the prototype. For instance, a basic dimensional analysis can be undertaken here to interpret the results of model tests in terms of prototype results. The principal parameters dominating the behavior of geocell-reinforced systems can be taken as:

$$f\left(B,L,\gamma, E_s, e, h, u, b,b_g, \emptyset, G\right) \tag{1}$$

where $f$ is a function of the systems, $B$ represents the width of the footing, $L$ is the length of the footing, $\gamma$ is the unit weight of the soil or footing, $E_s$ is the secant tensile stiffness of geocell material, $e$ stands for eccentricity, $h$ is the height of geocell, $u$ is the embedment depth of geocell, $b$ is the width of geocell layer, $b_g$ is the pocket width of geocell, $\emptyset$ is the internal friction angle of soil and $G$ is the shear modulus of soil.

The Buckingham [30] π dimensionless parameters can be expressed as π1, π2, π3, ..., π9 based on Langhaar's [11] theory. The independent variables obtained from the dimensional analysis within the function $g$ are as follows:

$$g(\pi_1,\pi_2,\pi_{3,\dots}\pi_9) = \left[\left(\frac{L}{B}\right),\left(\frac{E_s\gamma}{G^2}\right),\left(\frac{e}{B}\right),\left(\frac{h}{B}\right),\left(\frac{u}{B}\right),\left(\frac{b}{B}\right),\left(\frac{b_g}{B}\right),\left(\frac{G}{B\gamma}\right), \emptyset\right] \tag{2}$$

The scale factor ($n$) can be calculated using Eq. (3), which compares the geometries of the model and the prototype:

$$\frac{B_p}{B_m} = \frac{L_p}{L_m} = \frac{e_p}{e_m} = \frac{h_p}{h_m} = \frac{u_p}{u_m} = \frac{b_p}{b_m} = \frac{b_{g_p}}{b_{g_p}} = n \tag{3}$$

where subscript $p$ and $m$ stand for prototype and model, respectively. Buckingham's [30] dimensionless parameters must be equal in both the prototype and the model. Assuming that the unit weights ($\gamma$), Poisson's ratio ($\upsilon$) and internal friction angle ($\phi$) of the soils in the model

and prototype are the consistent between the model and prototype – an assumption supported by the findings of Sireesh et al. [31] – the ratio of elastic and shear modulus of the soil between the model and prototype can be expressed as follows:

$$(\pi_8)_m = (\pi_8)_p \Rightarrow \frac{G_m}{B_m \gamma_m} = \frac{G_p}{B_p \gamma_p} \Rightarrow \frac{E_m}{2(1+\upsilon_m) B_m \gamma_m} = \frac{E_p}{2(1+\upsilon_p) B_p \gamma_p} \Rightarrow \frac{G_m}{G_p} = \frac{E_m}{E_p} = \frac{B_m}{B_p} = \frac{1}{n} \quad (4)$$

and if

$$(\pi_2)_m = (\pi_2)_p \Rightarrow \frac{E_{sm}\gamma_m}{G_m{}^2} = \frac{E_{sp}\gamma_p}{G_p{}^2} \Rightarrow \frac{E_{sm}}{E_{sp}} = \frac{G_m{}^2}{G_p{}^2} = \frac{1}{n^2} \quad (5)$$

where, $E$ represents modulus of the soil.

According to Eq. (5), it is crucial to ensure that the tensile stiffness of the geocell in model tests is $n^2$ times lower than that of its large-scale prototype to avoid overestimating the improvement effect, as previously mentioned by several researchers [12,13,21,25,32-35]. However, even with rigorous dimensional analysis, there is a notable limitation when using conventional geocells in small-scale experiments. The geocell utilized in small-scale experiments often simulate prototype materials with exceptionally high tensile strength and secant stiffness, which are not used in real-world applications. As a result, the small-scale tests may significantly overestimate the effectiveness of geocells in enhancing footing systems.

In the present study, 3D-printed geocells scaled by a factor ($n$) of 3 were utilized to address these challenges mentioned in above paragraphs and provide a more accurate representation of field conditions in model tests. The scaling method used in this study was designed to represent prototype structures that are threefold larger geometrically ($n$=3) and ninefold ($n$=$3^2$) greater in secant tensile stiffness of geocell compared to their corresponding model tests. For example, a model test with a foundation width ($B$) of 100 mm and reinforced with a geocell having a secant tensile stiffness of 50 kN/m would correspond to a prototype structure, such as the foundation of a strip footing or a retaining wall, with a width of 300 mm ($B$ = 100 mm x 3) and reinforced with a geocell having a secant tensile stiffness of 450 kN/m ($E_s$=50 kN/m x 9).

## 3. Model geocell and 3D-printing

### *3.1. 3D-printer and filament selection*

A commercially available 3D-printer was used to produce scaled geocell models in terms of both geometry and material properties, aiming to represent the behavior of prototype fabricated geocell systems. The printer has a print volume of 220 x 220 x 250 mm, a single 0.4 mm nozzle, 1.75 mm filament size and a maximum print speed of 180 mm/s. It feasibly works with a wide range of available filaments, including polylactic acid (*PLA*), acrylonitrile butadiene styrene (*ABS*), polyethylene terephthalate (*PETG*), and thermoplastic polyurethane (*TPU*). Prior to initiating the 3D printing process, preliminary studies were conducted to understand the capabilities of each filament and to determine the best way to simulate the behavior of the prototype. All filaments, except for *TPU,* exhibited higher strength and lower strain at break than the fabricated geocells under tensile tests, indicating brittle characteristics. Conversely, *TPU* specimens displayed smooth and incremental increases in strength with elongation at lower levels, closely matching the behavior of fabricated *HDPE* geocells, yet exhibiting lower values. This difference in behavior was particularly relevant to our study objectives, which

focused on the scaling of geocell materials. Consequently, further studies focused on *TPU*, the filament with the lowest commercially available tensile strength.

### *3.2. Tensile strength/stiffness of model geocells*

Laboratory loading tests reveal that the modulus of elasticity of the geocell is a paramount factor influencing the behavior of geocell-reinforced foundations [1,36]. Specifically, a higher elastic modulus in the cellular structural element correlates with increased bearing capacity and system rigidity [22,23,25,37]. Researchers have used various index tests to analyze the stress-strain characteristics of geocells as reinforcement elements. ASTM D4595-17 [38] used by Refs. [39,40] and ASTM D6637-11 [41] used by Refs. [42-45] for geogrid-based geocells and ASTM D4884-09 [46] used by Ref. [45] for bodkin joints were used to examine the mechanical properties of geocells. Additional standards [47-49] were applied to analyze the mechanical properties of both commercially or hand-made geocells [10,24,50-53].

The reinforcement element may undergo tensile failure due to uneven loading or excessive deformation under footing loading [54-55]. Therefore, in this study, the cell-wall tensile stiffness and strengths according to ISO 527 [56] (dog-bone) and ISO 10319 [57] (wide-width) have been conducted to assess the strength characteristics of the geocell when considering evaluating proper scaling. These tests can be used to investigate the performance of a 3D-printed model geocell compared to a prototype for the potential failure modes for loading scenarios.

The initial step of this study was to design dog-bone samples using CAD software and fabricating them with *TPU* filaments via 3D printing. These samples were then compared with their counterparts, which were cut from the wall of a traditionally fabricated geocell. It has been noted that the strength of a 3D-printed model is proportional to the infill rate, an adjustable parameter controlling the density during printing [58]. Consequently, the samples were produced with infill rates of 5%, 10% and 20% to investigate the impact of infill on the strength of the model material. It should be noted that a minimum infill rate of 5% was established regarding printing technique and material integrity.

In order to examine the stress-strain relationship of prototype and model printed geocell dog-bone specimens, the overall and gauge lengths of 170 mm and 75 mm, respectively, were prepared according to ISO 527 [56]. Tensile tests were carried out a 30 kN capacity universal testing machine at a strain rate of 1% per minute under 23.1 $^{o}$C at a humidity of 48% (Fig. 1).

**Fig. 1.** Tensile stress vs. strain curves of dog-bone specimens for fabricated prototype and 3D-printed materials with 5% filling rate, along with a 1:9 scaled curve for the fabricated prototype.

The tensile stress-strain curves for dog-bone shape specimens, including a fabricated prototype and a 3D-printed material with a 5% filling rate, are illustrated in Fig. 1 with a benchmark of the scaled prototype at 1:9 (1:$n^2$). The tensile stress-strain relationships of the materials did not show a clear elastic region; thereby, the secant tensile stiffness, $E_{s(prototype)}$, of the fabricated material and the secant tensile stiffness, $E_{s(model)}$, of 3D-printed model material (*TPU*) were used for subsequent comparisons, as recommended by existing literature [47,59].

This comparison was based on the slope of the tangents to the tensile stress-strain curves at specific stress levels, namely at 2% and 5% strain rates. These rates are generally reasonable in field applications and model tests involving geocells [26,60,61]. The results indicated that the ratio $E_{s(prototype)}/E_{s(model)}$ was 9 at 2% stain and 7.3 at 5% strain levels. Additionally, the behavior of the model material of *TPU* closely resembled that of the prototype when scaled at 1:9.

Using a 100 mm width test specimen according to ISO 10319 [57] (wide-width) can result in a much more design-oriented value than test results from dog-bone specimens. Therefore, the tensile properties of the geocell materials were also evaluated using wide-width tensile tests on 100 mm wide prototype specimens and scaled 1:3 specimens of 33.3 mm width. These tests were conducted in a controlled environment of 47% humidity and a temperature of 23.4°C, employing a universal tensile testing machine. The strain rate was set at 20 ± 5% per minute. The potential for necking—induced by a higher length-to-width ratio—was not prominently observed during the tests while the specimen size requirements of ISO 10319 [57] could not be followed here for the scaled materials. Moreover, this study primarily focused on material behavior at low strain levels (i.e., $\varepsilon$= 2%), making any potential necking at higher strains less relevant to the analysis. Validation tests further confirmed that varying the specimen width from 33.3 mm to 66.6 mm did not significantly alter the tensile stress-strain behavior of the scaled material.

The tensile stress-strain curves of wide-width specimens, which include a fabricated prototype, a 3D-printed material with a 5% filling rate and a 1:9 scaled prototype, are presented in Fig. 2. Compared to prior tests using dog-bone shaped samples, these experiments indicated slightly higher values at lower strain levels. Specifically, the ratio of $E_{s(prototype)}/E_{s(model)}$ was measured at 13 for a 2% strain. However, the data converged towards a greater similarity at a 5% strain rate. Thus, 3D-printed geocells using *TPU* filaments appear to be effective, though not perfect, for scaling model geocells, achieving a specified scale factor ($n$) of 3.

**Fig. 2.** Tensile stress vs. strain curves of wide-width specimens for fabricated prototype and 3D-printed materials with 5% filling rate, along with a 1:9 scaled curve for the fabricated prototype.

## 4. Laboratory tests

### *4.1. Materials*

#### *4.1.1. Soil*

The soil classified as poorly graded sand (*SP*) per the Unified Soil Classification Systems (*USGS*) was used in the model tests. Its minimum ($e_{min}$) and maximum void ratios ($e_{max}$) are 0.57 and 0.83, respectively. Internal friction angles of the sand were obtained at relative densities of 35% and 75%, determined from a set of direct shear tests under normal stress of 50, 100 and 200 kPa. The details of the sand properties are given in Table 1.

**Table 1** The soil properties used in the experiments.

Preliminary tests were conducted to determine the required amount of soil, tamping height and number of tamping required to achieve a given relative density in the test tank. A relative density ($D_r$) of 35% was achieved without tamping for tests on loose sands. In the case of dense sand, the soil was leveled in the tank and gently tamped with a wooden tamper until achieving a relative density ($D_r$) of 75%. The relative density of each soil layer was checked using the sand cone method [68] and aluminum sample bowls. The variation in the relative density was typically within ±2–3%.

#### *4.1.2. Model and prototype geocells*

The fabrication of the 1:3 scaled 3D-printed geocells began with creating a design in CAD software. The model geocell was then created using a 3D printer, as illustrated in Fig. 3. Each printing session produced a 4-cell pattern arranged in a 2 x 2 configuration, approximately 140 x 164 mm, with each session taking about 4 hours to complete. A total of 16 cells in 2 x 2 configurations were produced. The fabrication process in the 3D printer was optimized to produce the largest possible geocell layer in a single printing session, constrained by the size of the 3D printing machine. These cells were subsequently bonded using epoxy glue under the assumption that the adhesive strength of the cell junction would exceed that of the cell walls, consistent with the behavior of the fabricated geocells. This approach was chosen to minimize the number of connections needed with epoxy glue and to expedite the printing process.

**Fig. 3.** Fabrication of 1:3 scaled model geocells through 3D printing.

The properties of the fabricated and 3D-printed model geocells used in the experiments are presented in Table 2. The geocells were 3D-printed in rectangular for the sake of production simplicity. However, the difference in effective opening area between the 3D-printed rectangular shape and the ideal honeycomb shape was negligible. Supporting this, Sherin et al. [51] found that footings reinforced with both honeycomb and rectangular shape geocells exhibited similar pressure-settlement behavior, provided that the geocells were fabricated from the same material and had identical opening areas, cell heights and widths. In summary, the dimensions of the model geocell resembled a good, though not perfect, geometric scaling of the prototype fabricated material in terms of appearance, dimensions and secant tensile stiffness.

**Table 2** Physical and mechanical properties of fabricated and scaled 3D-printed model geocells.

### *4.2. Test set-up*

The model tests were conducted in a tank with dimensions of 1000 mm in width, 1000 mm in length and 700 mm in height (Fig. 4). A steel footing with 100 mm in width, 996 mm in length and 20 mm in thickness was used in the experiments. The footing was centered in the test tank and its proper placement on the ground surface was verified using a spirit level. A 2 mm gap was also maintained between the ends of the footing and the tank to prevent any

undesirable interactions. The footing and the tank dimensions were carefully selected to minimize boundary effects. Cone-shaped grooves were opened on the footing to enable the application of various load eccentricities ($e$) of 0 (centric) and 1/6 (on the kern boundary) relative to the footing width ($B$).

**Fig. 4.** Schematic representation of the experimental setup.

### *4.3. Instrumentation*

The instrumentation used for the model tests included a hydraulic press, a load cell, linear voltage displacement transducers (*LVDTs*) and a data logger system. A hydraulic press with a 200 kN capacity was used to apply normal pressure to the footing. A compression-type load cell with a 200 kN capacity measured the normal pressure exerted on the footing. Displacements of both the footing and the soil surface throughout the tests were monitored using *LVDTs*, which had a stroke capacity of 100 mm and an accuracy of ±0.05%. All of these devices were connected to an 8-channel data logger, which enabled raw data transmission at 8 samples per second on each channel. Before each test, all measurement devices were calibrated to ensure precise and accurate measurements.

### *4.4. Test program*

A total of 12 static loading tests outlined in Table 3 were conducted to investigate the scale effects on the performance of centrically and eccentrically loaded strip footings on fabricated or 3D-printed geocell-reinforced sandy soils. The ratio of geocell embedment depth ($u$) and the geocell laying width ($b$) to width of foundation ($B$ = 100 mm), determined by averaging the optimum values obtained from previous experiments performed on geocell-reinforced strip footings [7,22,37,39,40,51,69-73], were kept constant as 0.1 and 8, respectively, in all tests. At least half of the tests were conducted multiple times to ensure the consistency and reliability of the data collected.

**Table 3** Experimental test program.

## 5. Results and discussions

### *5.1. Pressure-settlement performance and failure mechanisms*

The detailed set of footing pressure-settlement curves, covering both unreinforced and 3D-printed or fabricated geocell-reinforced loose and dense sands obtained from directly laboratory tests, is illustrated in Fig. 5 under both centric and eccentric loading conditions. The results revealed that the strip footing on sandy soil reinforced with fabricated geocells exhibited better pressure-bearing performance and initial stiffness of the footing bed than those reinforced with 3D-printed geocells, as expected. One contributing factor to the diminished performance of

scaled geocell models was a reduction in the confinement effect provided by geocells per unit volume of soil due to reduced material secant tensile stiffness ($E_s$), geocell height ($h$) and pocket width ($b_g$). Moreover, the reduced dimensions led to a smaller frictional surface area between geocells and soil particles, further decreasing the pressure-bearing capacity of the 3D-printed reinforced footing systems. Generally, the performance of the reinforced footing systems was influenced by eccentric loading and the relative density of the soil.

The punching failures with no well-defined failure points were observed in all cases for loose sand. The pressure-settlement curves of the footings for unreinforced and reinforced loose sand with either fabricated or 3D-printed geocells exhibited almost linear behavior up to about 30 mm of settlement under centric and eccentric loading of 1/6 (Fig. 5a). The surface settlement, rather than heave, was noted throughout the experiments. Furthermore, the diminishing impact of eccentricity on the bearing pressures was less pronounced in the fabricated geocell-reinforced soil compared to the 3D-printed geocell-reinforced soil. It was observed that the friction between the soil and the geocell layer was eventually overcome at both ends, which resulted in a concave deformation profile, as shown in Fig. 5a. This behavior was particularly noticeable in the case of 3D-printed geocells, as illustrated in Fig. 6a for an eccentricity ratio ($e/B$) of 1/6.

The ultimate bearing capacity of the strip footings on unreinforced dense sand was clearly defined under both centric and eccentric loading conditions, indicating the occurrence of traditional general shear failure, as demonstrated in Fig. 5b. Specifically, footings reinforced with fabricated geocells in dense sand demonstrated a strong strain-hardening response under centric loading, which is defined as a local shear failure. In these cases, the pressure progressively increased with increasing settlement. However, strain softening behavior was observed under eccentric loading of 1/6, corresponding to a general shear failure. On the other hand, footings reinforced with 3D-printed geocells exhibited weak strain-hardening behavior under both centric and eccentric loading of 1/6. It should be noted that the surface settlement/heave observations revealed differences in the anchoring effect between the two types of geocells. The fabricated geocells exhibited a stronger confining effect, which manifested in less surface heave compared to the 3D-printed geocells in the case of dense sand (see Fig. 6b).

**Fig. 5.** Bearing pressure-settlement results obtained directly from the strip footings on unreinforced, 3D-printed and fabricated geocell-reinforced for: (a) loose sand ($D_r$ = 35%) and (b) dense sand ($D_r$=75%).

**Fig. 6.** Surface displacement profiles of 3D-printed and fabricated geocell reinforced strip footing under an eccentricity ratio of 1/6 in: (a) loose sand and (b) dense sand.

In this study, the pressure-settlement behavior noted in fabricated geocells corresponds with the findings of small-scale tests conducted by various researchers [7,22,37,43,71,72,74-79]. This alignment is particularly evident when footings, reinforced with these geocells in dense sand, display a pronounced strain-hardening response, characterized by a steady increase in pressure concurrent with settlement under centric loading. Conversely, footings reinforced with

3D-printed geocells showed weak strain-hardening behavior under similar loading conditions, a trend that is consistent with large-scale test observations reported by Refs [18,19,80].

### *5.2. Improvement factor*

The settlement of the footing ($s$) and load eccentricity ($e$) can be normalized to the width of the strip footing ($B$), yielding non-dimensional factors of $s/B$ in percentage and $e/B$. An improvement factor ($I_f$) was also introduced to assess the effect of reinforcement on footing performance. Utilizing these non-dimensional parameters allows a more straightforward comparison of the experimental results. The improvement factor is defined as follows in Eq. (6):

$$I_f = \frac{q_r}{q_u} \tag{6}$$

where $q_r$ and $q_u$ represent the bearing pressures for the reinforced and the unreinforced soil, respectively, evaluated at the same relative density of the soil and a specific settlement level. If improvement factor is calculated at a settlement exceeding the ultimate capacity of unreinforced soil, the ultimate bearing capacity of the footing, $q_{ult,}$ is used instead of $q_u$.

The improvement factors for strip footings reinforced with either fabricated or 3D-printed geocells obtained from directly laboratory model tests are presented in Fig. 7. The use of fabricated geocells in small-scale tests resulted in improvement factors that were up to 65% higher in both loose and dense soils compared to those using scaled 3D-printed geocells. This circumstance arose from the greater apparent cohesion observed in soils confined by traditionally fabricated geocells compared to those confined by 3D-printed geocells [25,45,53,81]. Also, the higher secant tensile stiffness of the fabricated or unscaled geocell contributed to improved confinement of the sandy soil [22,23,25,37]. These observations are consistent with the findings of Fazeli Dehkordi and Karim [80], who noted a more substantial increase in improvement factors in small-scale tests compared to large-scale tests, especially when the $s/B$ ratio exceeded 10%. Furthermore, it was observed that increasing $s/B$ and $e/B$ ratios increased the improvement factor in both types of geocells. Similar results were reported by Jahanian et al. [73] for geogrid-based geocell reinforced strip footings.

**Fig. 7.** Improvement factors obtained directly from laboratory tests for footings reinforced with fabricated or 3D-printed geocells under centric and eccentric loading of 1/6 in (a) loose and (b) dense sand.

To comprehensively assess the effects of scaling on the improvement factors ($I_f$), the values of $I_f$ reported in various studies are summarized in Table 4. Although it's acknowledged that $I_f$ can be affected by multiple variables – such as soil properties, geocell material and aspect ratios – this evaluation specifically targeted scenarios where the footings were reinforced with traditional geocells in sandy soils, under centric loading and optimized test parameters by the researchers. Moreover, the analysis intentionally focused on more practical, allowable settlement levels, with an $s/B$ ratio of up to 20%, even though some studies [22,82] reported $I_f$ values as high as 9 at extremely high $s/B$ ratios.

**Table 4** Comparison of improvement factors ($I_f$) for footings on geocell-reinforced sand at varying settlement ratios ($s/B$), as reported in various studies.

Based on data gathered from existing literature and summarized in Table 4, the approximate upper and lower boundaries of the improvement factors for geocell-reinforced footings are illustrated in Fig. 8. In the examined literature, $I_f$ values for large-scale or field experiments were generally consistent and typically fall within the range of 1.1 to 1.6 while small-scale tests often resulted in significantly higher and more scatter values, reaching up to 7.5 at a $s/B$ ratio of 20%. Moreover, in small-scale tests, there was a more pronounced increase in these values with an increase in the $s/B$ ratio compared to the large-scale tests. Importantly, the $I_f$ values obtained in the present study using 3D-printed geocells are within the range of those reported for large-scale tests in the literature, thereby validating the accuracy of the scale-law predictions.

**Fig. 8.** Approximate upper and lower boundaries of improvement factors against settlement ratios from small- and large-scale tests in existing literature, with data points from the present study.

### *5.3. Verifying test results and modeling large-scale prototype*

In this study, the fabricated and 3D-printed geocell reinforced footing systems were simulated via PLAXIS 3D finite element (*FE*) software to verify the footing pressure-settlement responses of the small-scale experimental tests for 3D-printed and fabricated geocells conducted as part of this research. Following successful verification, these small-scale models were scaled up to examine how closely the 3D-printed geocell reinforced systems represent the behavior of their prototype counterparts according to scale factors based on Section 2. In the *FE* analysis for the prototype model, the scale factor of 3 ($n$) resulting from the performed dimensional analysis was applied to enlarge the dimensions of the test tank, 3D-printed geocell, and footing, as well as the embedment depth of geocell, modulus of the sandy soils and footing. Meanwhile, a scale of 9 ($n^2$) was used to enlarge the secant tensile stiffness of the 3D-printed geocell. Furthermore, for the prototype-scale, the Poisson ratio, unit weight, as well as cohesion, dilatancy angle, failure ratio, exponential power values, were selected to be consistent with the values preferred for small-scale modelling. In addition to the scaling procedures described, the finite element analyses were also accounted for potential unexpected parameters that could influence the behavior of the geocell-reinforced systems in field conditions, ensuring a more robust and realistic simulation of both small-scale and prototype-scale models. The specified parameters in numerical analyses for both the small-scale and prototype-scale models are given in Table 5.

**Table 5** Material properties used for validating numerical models of geocell-reinforced systems: comparison of small-scale and prototype-scale (field condition).

In the numerical simulations conducted for this study, the properties of sandy soil were represented using the Hardening Soil (*HS*) constitutive model. This stress-dependent elastoplastic model accurately represents the nonlinear behavior of sandy soils, offering an improvement over elastic perfectly plastic models [90]. Parameters for the *HS* model were calibrated using the results of small-scale laboratory tests. *HS* model accurately simulated the stress-strain behavior of soil up to its peak shear strength, although it did not capture the post-peak softening behavior of the soil. It should be noted that a low cohesion (*c*) value of 1 kPa was selected for the *HS* model to prevent early soil yielding in areas with low confining pressures [91-93].

The strip footing was modelled as a linear elastic plate structural element in the numerical analyses using conventional steel parameters for Young's modulus and Poisson's ratio. Similarly, several researchers [91,92,94-98] have recommended to use plate structural element for footing modelling. In the simulation, the fabricated geocells were built in CAD software and imported into PLAXIS 3D while 3D-printed geocells were directly constructed within the *FE* software environment. The fabricated and 3D-printed geocells were represented as geogrid structural elements, which were isotropic elastoplastic materials characterized by axial stiffness (*EA*) but no bending stiffness. This modeling choice aligns with the approach taken by several researchers [95-99]. The axial stiffness values for the geocells were determined using the tensile stress-strain curves obtained in Fig. 1 according to ISO 527 [56]. Additionally, 12 node interface elements were used to model the interaction between soil and geocells, highlighting the interface's partially bonded character with a reduction factor ($R_{int}$) of 0.8. The approach aligns with parameters used in the studies by Refs. [16,99].

A predefined line load was applied to the model until the simulated footing reached the point of failure. It is important to note that the softening behavior observed after general shear failure in the pressure-settlement response of unreinforced dense sand cannot be directly modeled within the constraints of the *HS* constitutive model. Despite this limitation, the *HS* model was adept in capturing the essential aspects of soil behavior, particularly in alignment with the settlements observed during our experimental tests. In numerical modeling, clusters were divided into mesh a with 10-node tetrahedral elements and three nodes. Moreover, a series of trial-and-error mesh sensitivity analyses were carried out. Based on these analyses, an average mesh size of 0.08 m was chosen to verify small-scale test results while a mesh size of 0.17 m was selected for the prototype-scale. The *FE* model geometry, which includes the strip footing, fabricated or 3D-printed geocells and the line loads, are illustrated in Fig. 9.

**Fig. 9.** Numerical models of reinforced strip footings with (a) fabricated and (b) 3D-printed geocells under centric loading.

The pressure-settlement results of the footings on the unreinforced sand, reinforced sand with fabricated and 3D-printed geocell are presented in Fig. 10, based on laboratory model test data and numerical results. It was observed that the numerical results generally consisted of the outcomes of small-scale tests conducted on sandy soils of varying relative densities and reinforcement types, namely 3D-printed and fabricated geocells. Notably, minor discrepancies between laboratory tests and numerical results were observed in the pressure-settlement

responses for both unreinforced and reinforced dense sand when subjected to eccentric loading. These variations could arise from the complex stress distribution introduced by eccentric loading, which the finite element model may not fully capture due to inherent simplifications. In addition, the footing pressure-settlement results in numerical modeling for both 3D-printed and fabricated geocells were lower than the test outcomes in loose sand conditions. The slight inconsistency between the finite element model outcomes and the actual test results could be attributed to limitations in accurately capturing the complex soil-geocell interactions in a loose sand environment. In general, the calibrated models have demonstrated sufficient accuracy to justify their use in simulating prototype models.

**Fig. 10.** Test results of small-scale laboratory tests verified with FE method for strip footings on (a) unreinforced and (b) 3D-printed and fabricated geocell reinforced sands under centric and eccentric loading of 1/6.

Caution must be exercised when extrapolating the finding of small-scale model tests to large-scale prototypes even if properly scaled 3D-printed geocells are employed in small-scale model tests and applying dimensional analysis. Such extrapolations may result in non-conservative estimates of improvement factors, potentially influenced by scale effects such as variations in footing width, geocell sizes and changes in failure mechanisms. To address these complexities, further numerical analyses were carried out to assess the representativeness of the 3D-printed small-scale test results for large-scale or prototype conditions, along with the validated experimental results. In this context, unreinforced and reinforced loose and dense sands under centric loading were modeled at the prototype scale. The parameters used for the 1:3 scaled small-scale models and their corresponding large-scale prototypes are detailed in Table 5.

The improvement factors obtained from numerical analyses for both small-scale and prototype models involving unreinforced and 3D-printed geocell-reinforced soils in loose and dense sands under centric loading are presented in Table 6. As the footing width ($B$) increased, the corresponding back-calculated bearing capacity factors ($N_\gamma$) decreased for unreinforced and reinforced conditions in prototype modeling. This phenomenon aligns with previous studies, which attribute the decline to variations in mean stress beneath the footing as the footing width increases [18,19,97,100,101]. More importantly, a comprehensive assessment of pressure-settlement responses was also carried out, revealing a consistent trend between 3D-printed geocell models and their corresponding large-scale counterparts, as illustrated in Fig. 11. A noteworthy discrepancy was observed in the case of 3D-printed geocell reinforced loose sand. The numerical model could not replicate the geocell layer's concave deformation under footing loading, which was observed in the experimental tests. This may be attributed to reduced vertical frictional forces acting on the geocell walls in numerical modeling. Thus, the finite element model did not perfectly capture the membrane mechanism of the geocell in loose sand conditions. This mechanism involved geocell deflection, which generated additional tensile forces, leading to a more noticeable reduction in footing pressure. Despite this exception, in the case of dense sand conditions, the improvement factors exhibited similar results between small-scale and prototype models, as detailed in Table 6. Therefore, the findings illustrated that the diligent application of dimensional analysis and the precise scaling of the key parameters in reinforced footing systems using 3D-printed geocells can make small-scale tests reliable for extrapolating large-scale behavior.

**Fig. 11.** Comparison of small-scale and prototype-scale numerical analyses with experimental test results of 3D-printed geocell-reinforced footing under centric loading.

**Table 6** Improvement factors for 3D-printed geocells and prototype numerical models at a settlement (*s*) of 10 mm.

A comparative analysis of incremental deviatoric strain in dense sand under centric loading for small-scale and prototype-scale models is also illustrated in Fig. 12 with and without 3D-printed geocell reinforcement. In general, failure mechanisms and the borders of the heave from the footing axis were largely consistent across both scales for unreinforced and reinforced dense sands. It should be noted that a more widespread settlement pattern was noted in the case of the reinforced soil in both small-scale and prototype models. This can be attributed to the significant role of the geocell layer in effectively confining the sand and distributing the applied axial load over larger areas due to its stress distribution mechanism, leading to beam-like deformation under the footing loading.

**Fig. 12.** Distribution of incremental deviatoric strain for dense sand under centric loading (a) unreinforced small-scale, (b) 3D-printed geocell reinforced small-scale, (c) unreinforced prototype and (d) 3D-printed geocell reinforced prototype.

## 6. Conclusion

In this study, it is aimed to systematically investigate the performance of strip footings reinforced with both traditional fabricated and 3D-printed geocells to address the persistent challenge of scaling in the field of geocell-reinforced systems. Initially, scaled geocell models were produced using 3D printing technology and carefully selected filaments, where geometry and model stiffness were accurately scaled using scaling laws. The model tests were also conducted to compare the strip footings reinforced with fabricated or 3D-printed geocells in terms of the footing pressure-settlement responses, surface displacement characteristics and improvement factors under both centric and eccentric loading conditions in loose and dense sands. The experimental findings were further validated and extended to large-scale prototype models through numerical analyses. The main conclusions are summarized as follows:

- 3D printing technology has enabled the creation of geocells that were scaled in both geometric dimensions and material properties, offering a flexible and accurate approach to study the effects of scaling in model tests. Specifically, a stress-strain relationship similar to that of large-scale geocells was successfully achieved in the model geocell, making them suitable for 1:3 scaled reinforced-soil model tests in 1-g conditions. This innovation highlights the promising advantages of 3D-printed geocells in customization and rapid prototyping.
- In the existing literature, the improvement factors derived from small-scale tests are generally higher than those obtained from large-scale tests. These findings suggest the

extent to which the improvement effect could be exaggerated if scale effects are not properly considered. In this study, the observed improvement factors in the performed experiments using 3D-printed geocells closely aligned with those from large-scale tests in the literature, corroborating the validity of scale-law expectations. On the other hand, footings reinforced with fabricated geocells in model tests yielded improvement factors up to 65% higher than those using 3D-printed geocells across both loose and dense soils in model tests.

- The model test results were further validated through various 3D numerical analyses, which demonstrated that the performance of scaled footings using 3D-printed geocells closely aligned with numerical models. Once validated, these finite element models were proportionally scaled up to assess the representativeness of 3D-printed geocell systems in relation to large-scale prototypes. An in-depth evaluation of footing pressure-settlement responses illustrated a consistent pattern between 3D-printed geocell models and their large-scale equivalents, resulting in similar improvement factors for each case. However, the numerical models could not completely capture a specific concave deformation behavior observed in 3D-printed geocell-reinforced loose sand. This indicates the model's restricted capacity to simulate complex load-transfer and stress distribution mechanisms in reinforced loose sand. Despite this shortcoming, the study reaffirms that 3D-printed geocells in small-scale tests offer valuable insights into predicting large-scale behaviors and their improvement factors when accompanied by thorough dimensional analysis and considerations of scale effects.

This study has opened new pathways for future research in applying 3D-printed geocells in soil reinforcement. One such direction involves evaluating a broader range of materials for 3D printing to capture a more detailed set of geocell physical and mechanical properties. Expanding the scale investigations to encompass various foundation types, soil conditions, and loading scenarios would also be valuable. Furthermore, more sophisticated 3D numerical simulations are essential to demonstrate the level of accuracy with which 3D-printed models can represent large-scale behavior across these diverse conditions.

While our findings affirm the utility of 3D-printed models for simulating large-scale behavior, it's crucial to note that the reinforcement effect in loose sand was not adequately captured in the numerical models. This limitation implies that caution is necessary when using finite element analysis for modeling geocell-reinforced loose sand in real-case scenarios, as current simulations may not fully capture the complex interactions and behaviors, potentially leading to inaccuracies in design and analysis. In the future studies, a more nuanced exploration of the interactions between sand particles and geocells, particularly the complex contraction behavior of sand and interface frictions, is crucial. Additionally, accurately representing the general concave behavior under loading, which current models struggle to capture, is essential. This requires a deeper understanding of how sand behaves at different relative densities when integrated with reinforcing materials, crucial for predicting and optimizing the performance of geotechnical applications.

**Acknowledgment**

The authors acknowledge the support and cooperation of Ferhat Karataş throughout the performed tests.

**CRediT authorship contribution statement**



Journal Pre-proofs

**Sarper Demirdöğen:** Conceptualization, Software, Investigation, Visualization, Writing - Original Draft **Ayhan Gürbüz**: Conceptualization, Writing - Review & Editing, Supervision **Kaan Yünkül:** Conceptualization, Investigation, Visualization, Writing - Review & Editing

**Declaration of competing interest**

The authors declare that they have no known competing financial interests or personal relationships that could have appeared to influence the work reported in this paper.

**References**

[1] Sitharam TG, Hegde AM, Kolathayar S. Geocells: advances and applications. Springer Transactions in Civil and Environmental Engineering; 2020.

[2] Vesic AS. Analysis of ultimate loads of shallow foundations. Journal of the Soil Mechanics and Foundations Division 1973;99(1):45-73. https://doi.org/10.1061/JSFEAQ.0001846.

[3] Ovesen NK. The use of physical models in design: the scaling law relationship. In Proceeding of 7th European Conference on Soil Mechanics and Foundation Engineering, Brighton, England; 1979. 4, p. 318–323.

[4] Yetimoglu T, Wu JT, Saglamer A. Bearing capacity of rectangular footings on geogrid-reinforced sand. Journal of Geotechnical Engineering 1994;120(12):2083-2099. https://doi.org/10.1061/(ASCE)0733-9410(1994)120:12(2083).

[5] Krishnaswamy NR, Rajagopal K, Latha GM. Model studies on geocell supported embankments constructed over a soft clay foundation. Geotechnical Testing Journal 2000;23(1):45-54. https://doi.org/10.1520/GTJ11122J.

[6] Wood DM. Geotechnical modelling. CRC Press, London, UK; 2004.

[7] Gurbuz A, Mertol HC. Interaction between assembled 3D honeycomb cells produced from high density polyethylene and a cohesionless soil. Journal of Reinforced Plastics and Composites 2012;31(12):828-836. https://doi.org/10.1177/0731684412447529.

[8] Hegde A. Geocell reinforced foundation beds-past findings, present trends and future prospects: a state-of-the-art review. Construction and Building Materials 2017;154:658-674. https://doi.org/10.1016/j.conbuildmat.2017.07.230.

[9] Isik A, Gurbuz A. Pullout behavior of geocell reinforcement in cohesionless soils. Geotextiles and Geomembranes 2020;48(1):71-81. https://doi.org/10.1016/j.geotexmem.2019.103506.

[10] Hegde AM, Palsule PS. Performance of geosynthetics reinforced subgrade subjected to repeated vehicle loads: experimental and numerical studies. Frontiers in Built Environment 2020;6:15. https://doi.org/10.3389/fbuil.2020.00015.

[11] Langhaar HL. Dimensional analysis and theory of models. New York: Wiley; 1951.

[12] Fannin RJ. Geogrid Reinforcement of Granular Layers on Soft Clay: A Study at Model and Full Scale. PhD Thesis, University of Oxford, England; 1986.

[13] Fakher A, Jones CJ. Discussion: bearing capacity of rectangular footings on geogrid-reinforced sand. Journal of Geotechnical Engineering 1996;122(4):326-327. https://doi.org/10.1061/(ASCE)0733-9410(1996)122:4(326).

[14] Butterfield R. Dimensional analysis for geotechnical engineers. Geotechnique 1999;49(3):357-366. https://doi.org/10.1680/geot.1999.49.3.357 .

[15] Sadoglu E. Numerical analysis of centrally and eccentrically loaded strip footing on geotextile-reinforced sand. Geosynthetics International 2015;22(3):225-234. https://doi.org/10.1680/gein.15.00007.

[16] Nasr AM, Azzam WR. Behaviour of eccentrically loaded strip footings resting on sand. International Journal of Physical Modelling in Geotechnics 2017;17(3):177-194. https://doi.org/10.1680/jphmg.16.00008.

[17] Hegde A, Sitharam TG. Experiment and 3D-numerical studies on soft clay bed reinforced with different types of cellular confinement systems. Transportation Geotechnics 2017;10:73-84. https://doi.org/10.1016/j.trgeo.2017.01.001.

[18] Shadmand A, Ghazavi M, Ganjian N. Load-settlement characteristics of large-scale square footing on sand reinforced with opening geocell reinforcement. Geotextiles and Geomembranes 2018a;46(3):319-326. https://doi.org/10.1016/j.geotexmem.2018.01.001.

[19] Shadmand A, Ghazavi M, Ganjian N. Scale effects of footings on geocell reinforced sand using large-scale tests. Civil Engineering Journal 2018b;4(3),497. https://doi.org/10.28991/cej-0309110.

[20] Yunkul K, Gurbuz A. Shaking table study on seismic behavior of MSE wall with inclined backfill soils reinforced by polymeric geostrips. Geotextiles and Geomembranes 2022a;50(1):116-136. https://doi.org/10.1016/j.geotexmem.2021.09.005.

[21] Sheikh IR, Shah MY. State-of-the-art review on the role of geocells in soil reinforcement. Geotechnical and Geological Engineering 2021;39:1727-1741. https://doi.org/10.1007/s10706-020-01629-3.

[22] Dash SK, Krishnaswamy NR, Rajagopal K. Bearing capacity of strip footings supported on geocell-reinforced sand. Geotextiles and Geomembranes 2001a;19(4):235–256. https://doi.org/10.1016/S0266-1144(01)00006-1.

[23] Lal D, Sankar N, Chandrakaran S. Behaviour of square footing on sand reinforced with coir geocell. Arabian Journal of Geosciences 2017;10,1-8. https://doi.org/10.1007/s12517-017-3131-9.

[24] Chen RH, Chiu YM. Model tests of geocell retaining structures. Geotextiles and Geomembranes 2008;26(1):56-70. https://doi.org/10.1016/j.geotexmem.2007.03.001.

[25] Kargar M, Hosseini SMMM. Effect of reinforcement geometry on the performance of a reduced-scale strip footing model supported on geocell-reinforced sand. Scientia Iranica 2017;24(1):96-109. https://doi.org/10.24200/SCI.2017.2380.

[26] Stathas D, Wang JP, Ling HI. Model geogrids and 3D printing. Geotextiles and Geomembranes 2017;45(6):688-696. https://doi.org/10.1016/j.geotexmem.2017.07.006.

[27] Arab MG, Omar M, Alotaibi E, Mostafa O, Naeem M, Badr O. Bio-inspired 3D-printed honeycomb for soil reinforcement. In Proceeding of Geo-Congress 2020 Reston, VA: American Society of Civil Engineers; 2020.

[28] Zhang M, Zhu H, Yang J, Qiu C, Javadi AA. Experimental study of a 3D printed geogrid embedded with FBG sensor for reinforcement of subgrade with underlying cave. Geotextiles and Geomembranes 2023;51(5):81-92. https://doi.org/10.1016/j.geotexmem.2023.05.001.

[29] Zeng WX, Ying MJ, Liu FY. Investigation on the cyclic shear response of stereoscopic geogrid-reinforced coarse-grained soil interface. Transportation Geotechnics 2023;38:100905. https://doi.org/10.1016/j.trgeo.2022.100905.

[30] Buckingham E. On physically similar systems; illustrations of the use of dimensional equations. Physical Review 1914;4(4):345. https://doi.org/10.1103/PhysRev.4.345.

[31] Sireesh S, Sitharam TG, Dash SK. Bearing capacity of circular footing on geocell–sand mattress overlying clay bed with void. Geotextiles and Geomembranes 2009;27(2):89-98. https://doi.org/10.1016/j.geotexmem.2008.09.005

[32] Love JP. Model testing of geogrids in unpaved roads. PhD Thesis, University of Oxford, England; 1984.

[33] Iai S. Similitude for shaking table tests on soil-structure-fluid model in 1g gravitational field. Soils and Foundations 1989;29(1):105-118. https://doi.org/10.3208/sandf1972.29.105.

[34] Viswanadham BVS, König D. Studies on scaling and instrumentation of a geogrid. Geotextiles and Geomembranes 2004;22(5):307-328. https://doi.org/10.1016/S0266-1144(03)00045-1.

[35] Yunkul K, Gurbuz A. Uplift behavior of shallow horizontal plate anchors reinforced with geocells in cohesionless soil. European Journal of Environmental and Civil Engineering 2022b;26(4):1243-1266. https://doi.org/10.1080/19648189.2019.1707123.

[36] Vega, E., Van Gurp, C., Kwast, E. Geosynthetics for reinforcement of unbound base and subbase pavement layers, SBRCURnet (CROW), Netherlands. CRW C1001; 2018 (in Dutch).

[37] Dash SK. Effect of geocell type on load-carrying mechanisms of geocell-reinforced sand foundations. International Journal of Geomechanics 2012;12(5):537-548. https://doi.org/10.1061/(ASCE)GM.1943-5622.0000162.

[38] American Society for Testing and Materials (ASTM). Standard test method for tensile properties of geotextiles by the wide-width strip method. ASTM D4595–17; 2017.

[39] Dash SK, Rajagopal K, Krishnaswamy NR. Performance of different geosynthetic reinforcement materials in sand foundations. Geosynthetics International 2004;11(1):35-42. https://doi.org/10.1680/gein.2004.11.1.35.

[40] Dash SK, Rajagopal K, Krishnaswamy NR. Behaviour of geocell-reinforced sand beds under strip loading. Canadian Geotechnical Journal 2007;44(7):905-916. https://doi.org/10.1139/t07-035.

[41] American Society for Testing and Materials (ASTM). Standard test method for determining tensile properties of geogrids by the single or multi-rib tensile method. ASTM D6637-11; 2015.

[42] Sitharam TG, Sireesh S. Effects of base geogrid on geocell-reinforced foundation beds. Geomechanics and Geoengineering 2006;1(3):207-216. https://doi.org/10.1080/17486020600900596.

[43] Latha GM, Somwanshi A. Bearing capacity of square footings on geosynthetic reinforced sand. Geotextiles and Geomembranes 2009;27(4):281-294. https://doi.org/10.1016/j.geotexmem.2009.02.001.

[44] Biswas A, Krishna AM, Dash SK. Influence of subgrade strength on the performance of geocell-reinforced foundation systems. Geosynthetics International 2013;20(6):376-388. https://doi.org/10.1680/gein.13.00025.

[45] Biswas A, Krishna AM, Dash SK. Behavior of geosynthetic reinforced soil foundation systems supported on stiff clay subgrade. International Journal of Geomechanics 2016;16(5):04016007. https://doi.org/10.1061/(ASCE)GM.1943-5622.0000559.

[46] American Society for Testing and Materials (ASTM). Standard test method for strength of sewn or thermally bonded seams of geotextiles. ASTM D4884-09; 2012.

[47] American Society for Testing and Materials (ASTM). Standard test method for tensile properties of plastics. ASTM D638-14; 2022.

[48] American Society for Testing and Materials (ASTM). Standard test method for determining tensile properties of nonreinforced polyethylene and nonreinforced flexible polypropylene geomembranes. ASTM D6693-04; 2015.

[49] American Society for Testing and Materials (ASTM). Standard Test Method for Determining Performance Strength of Geomembranes by the Wide Strip Tensile Method. ASTM D4885-01; 2023.

[50] Mengelt M, Edil TB, Benson CH. Resilient modulus and plastic deformation of soil confined in a geocell. Geosynthetics International 2006;13(5):195-205. https://doi.org/10.1680/gein.2006.13.5.195.

[51] Sherin KS, Chandrakaran S, Sankar N. Effect of geocell geometry and multi-layer system on the performance of geocell reinforced sand under a square footing. International Journal of Geosynthetics and Ground Engineering 2017;3:1-11. https://doi.org/10.1007/s40891-017-0097-3.

[52] Venkateswarlu H, Ujjawal KN, Hegde A. Laboratory and numerical investigation of machine foundations reinforced with geogrids and geocells. Geotextiles and Geomembranes 2018;46(6):882-896. https://doi.org/10.1016/j.geotexmem.2018.08.006.

[53] Fazeli Dehkordi P, Ghazavi M, Karim UFA. Bearing capacity-relative density behavior of circular footings resting on geocell-reinforced sand. European Journal of Environmental and Civil Engineering 2022;26(11):5088-5112. https://doi.org/10.1080/19648189.2021.1884901.

[54] Mitchell JK, Kao TC, Kavazanjian Jr E. Analysis of grid cell reinforced pavement base. Technical Report (No. GL-79-8), Department of Civil Engineering, University of California Berkeley, USA; 1979.

[55] Liu Y, Deng A, Jaksa M. Failure mechanisms of geocell walls and junctions. Geotextiles and Geomembranes 2019;47(2):104-120. https://doi.org/10.1016/j.geotexmem.2018.11.003.

[56] International Organization for Standardization (ISO). Plastics-Determination of tensile properties. ISO 527; 2019.

[57] International Organization for Standardization (ISO). Geosynthetics-wide-width tensile test. ISO 10319; 2015.

[58] Lee H, Eom RI, Lee Y. Evaluation of the mechanical properties of porous thermoplastic polyurethane obtained by 3D printing for protective gear. Advances in Materials Science and Engineering 2019;1-10. https://doi.org/10.1155/2019/5838361.

[59] Koerner RM. Designing with geosynthetics. 5th Edition. Pearson Prentice Hall, New Jersey, USA; 2012.

[60] Pokharel SK, Han J, Leshchinsky D, Parsons RL, Halahmi I. Investigation of factors influencing behavior of single geocell-reinforced bases under static loading. Geotextiles and Geomembranes 2010;28(6):570-578. https://doi.org/10.1016/j.geotexmem.2010.06.002.

[61] Isik A, Anil O, Gurbuz A. Proposed novel bond-slip model for geocell reinforcement under pull-out loading condition. Géotechnique 2022;1-13. https://doi.org/10.1680/jgeot.21.00120.

[62] American Society for Testing and Materials (ASTM). Standard practice for classification of soils for engineering purposes (unified soil classification system). ASTM D2487-17; 2020.

[63] American Society for Testing and Materials (ASTM). Standard test methods for specific gravity of soil solids by water pycnometer. ASTM D854-14; 2023.

[64] American Society for Testing and Materials (ASTM). Standard test methods for particle-size distribution (gradation) of soils using sieve analysis. ASTM D6913-04; 2022.

[65] American Society for Testing and Materials (ASTM). Standard test methods for maximum index density and unit weight of soils using a vibratory table. ASTM D4253-16; 2019.

[66] American Society for Testing and Materials (ASTM). Standard test methods for minimum index density and unit weight of soils and calculation of relative density. ASTM D4254-16; 2016.

[67] American Society for Testing and Materials (ASTM). Standard test method for direct shear test of soils under consolidated drained conditions. ASTM D3080-11; 2020.

[68] American Society for Testing and Materials (ASTM). Standard test method for density and unit weight of soil in place by sand-cone method. ASTM 1556-15; 2016.

[69] Dash SK, Reddy PDT, Raghukanth STG. Subgrade modulus of geocell-reinforced sand foundations. Proceedings of the Institution of Civil Engineers-Ground Improvement 2008;161(2):79-87. https://doi.org/10.1680/grim.2008.161.2.79.

[70] Latha GM, Dash SK, Rajagopal K. Numerical simulation of the behavior of geocell reinforced sand in foundations. International Journal of Geomechanics 2009;9(4):143-152. https://doi.org/10.1061/(ASCE)1532-3641(2009)9:4(143).

[71] Moghaddas Tafreshi S, Dawson AR. Comparison of bearing capacity of a strip footing on sand with geocell and with planar forms of geotextile reinforcement. Geotextiles and Geomembranes 2010;28(1):72-84. https://doi.org/10.1016/j.geotexmem.2009.09.003.

[72] Doley C, Das UK, Shukla SK. Development of a multiple regression equation for prediction of bearing capacity of geocell-reinforced sand beds based on experimental study. Arabian Journal of Geosciences 2022;15(16):1408. https://doi.org/10.1007/s12517-022-10652-y.

[73] Jahanian MS, Razmkhah A, Ghasemzadeh H, Vosoughifar H. Bearing capacity of the strip footing located on the sand reinforced by geocell under eccentric load. Arabian Journal of Geosciences 2022;15(15):1328. https://doi.org/10.1007/s12517-022-10600-w.

[74] Dash SK, Rajagopal K, Krishnaswamy NR. Strip footing on geocell reinforced sand beds with additional planar reinforcement. Geotextiles and Geomembranes 2001b;19(8):529-538. https://doi.org/10.1016/S0266-1144(01)00022-X.

[75] Dash SK. Influence of relative density of soil on performance of geocell-reinforced sand foundations. Journal of Materials in Civil Engineering 2010;22(5),533-538. https://doi.org/10.1061/(ASCE)MT.1943-5533.0000040.

[76] Hegde A, Sitharam TG. 3-dimensional numerical modelling geocell reinforced sand beds. Geotextiles and Geomembranes 2015a;43:171–181. https://doi.org/10.1016/j.geotexmem.2014.11.009.

[77] Hegde A, Sitharam TG. Experimental and numerical studies on protection of buried pipelines and underground utilities using geocells. Geotextiles and Geomembranes 2015b;43 (5),372–381. https://doi.org/10.1016/j.geotexmem.2015.04.010.

[78] Simsek MN. Behavior of geocell reinforced sandy soils under static load. Master Thesis, Middle East Technical University, Ankara, Turkey; 2017.

[79] Doley C, Das UK, Shukla SK. Response of square footing on geocell-reinforced sand bed under static and repeated loads. International Journal of Geosynthetics and Ground Engineering 2021;7(4):90. https://doi.org/10.1007/s40891-021-00336-0.

[80] Fazeli Dehkordi P, Karim UFA. Behaviour of circular footings confined by rigid base and geocell reinforcement. Arabian Journal of Geosciences 2020;13:1-12. https://doi.org/10.1007/s12517-020-06092-1.

[81] Hegde A, Sitharam TG. Experimental and numerical studies on footings supported on geocell reinforced sand and clay beds. International Journal of Geotechnical Engineering 2013;7(4), 346-354.

[82] Sitharam TG, Sireesh S, Dash SK. Model studies of a circular footing supported on geocell-reinforced clay. Canadian Geotechnical Journal 2005;42(2):693-703. https://doi.org/10.1139/t04-117.

[83] Moghaddas Tafreshi S, Sharifi P, Dawson AR. Performance of circular footings on sand by use of multiple-geocell or-planar geotextile reinforcing layers. Soils and Foundations 2016;56(6):984-997. https://doi.org/10.1016/j.sandf.2016.11.004.

[84] Kaur A, Gill KS, Singh P. Bearing capacity improvement using geocell reinforced sand. In: Proceedings of the 1st International Conference on Sustainable Waste Management through Design: IC_SWMD 2018, Springer International Publishing; 2018; 1,p. 160-169.

[85] Kargar M, Hosseini SMMM. Influence of reinforcement stiffness and strength on load-settlement response of geocell-reinforced sand bases. European Journal of Environmental and Civil Engineering 2018;22(5):596-613. https://doi.org/10.1080/19648189.2016.1214181.

[86] Li L, Xiao H, Gao M, Liu Y, Hu Z, Yao K. Experimental investigations on effect of geocell, waste tire chips, and geocell–tire chips on foundation reinforcement. Journal of Performance of Constructed Facilities 2019;33(6):04019074. https://doi.org/10.1061/(ASCE)CF.1943-5509.0001352.

[87] Muthukumar S, Sakthivelu A, Shanmugasundaram K, Mahendran N, Ravichandran V. Performance assessment of square footing on jute geocell-reinforced sand. International Journal of Geosynthetics and Ground Engineering 2019;5:1-10. https://doi.org/10.1007/s40891-019-0176-8.

[88] Portakal GG. Investigation of bearing capacity of geocell-reinforced soils with field tests. Master Thesis, İskenderun Technical University, Hatay, Turkey; 2021 (in Turkish).

[89] Sharma V, Kumar A. Behavior of eccentrically and obliquely loaded ring footing resting on geocell-reinforced sand. Innovative Infrastructure Solutions 2022;7(6):359. https://doi.org/10.1007/s41062-022-00961-2.

[90] Obrzud RF. On the use of the Hardening Soil Small Strain model in geotechnical practice. Numerics in Geotechnics and Structures 2010; 16, p. 1-17.

[91] Keskin MS, Laman M. Experimental and numerical studies of strip footings on geogrid-reinforced sand slope. Arabian Journal for Science and Engineering 2014;39:1607-1619. https://doi.org/10.1007/s13369-013-0795-7.

[92] Gupta S, Mital A. A comparative study of bearing capacity of shallow footing under different loading conditions. Geomechanics and Geoengineering 2022;17(4):1338-1349. https://doi.org/10.1080/17486025.2021.1940310.

[93] Safaee AM. Performance of the multi-tiered GMSE walls under seismic conditions: Comparison of physical and numerical simulations. Soil Dynamics and Earthquake Engineering 2022;159:107316. https://doi.org/10.1016/j.soildyn.2022.107316.

[94] Demir A, Yildiz A, Laman M, Ornek M. Experimental and numerical analyses of circular footing on geogrid-reinforced granular fill underlain by soft clay. Acta Geotechnica 2014;9:711-723. https://doi.org/10.1007/s11440-013-0207-x.

[95] Nadaf MB, Mandal JN. Numerical analyses of loaded strip footing resting on cellular mattress and strips: reinforced fly ash slope. International Journal of Geosynthetics and Ground Engineering 2017;3:1-16. https://doi.org/10.1007/s40891-017-0106-6.

[96] Chowdhury S, Patra NR. Settlement behavior of circular footing on geocell-and geogrid-reinforced pond ash bed under combine static and cyclic loading. Arabian Journal of Geosciences 2021;14(11):1063. https://doi.org/10.1007/s12517-021-07424-5.

[97] Yunkul K, Usluogullari OF, Gurbuz A. Numerical analysis of geocell reinforced square shallow horizontal plate anchor. Geotechnical and Geological Engineering 2021;39(4):3081-3099. https://doi.org/10.1007/s10706-021-01679-1.

[98] Dandin S, Kulkarni M, Wagale M. Fly Ash Based Subgrade Reinforced with Pet Bottles as Non-conventional Geocell: a 3D Finite Element Analysis. Geotechnical and Geological Engineering 2023;41(2):1537-1556. https://doi.org/10.1007/s10706-022-02352-x.

[99] Ari A, Misir G. Three-dimensional numerical analysis of geocell reinforced shell foundations. Geotextiles and Geomembranes 2021;49(4):963-975. https://doi.org/10.1016/j.geotexmem.2021.01.006.

[100] DeBeer EE. Experimental determination of the shape factors and the bearing capacity factors of sand. Géotechnique 1970;20 :387–411. https://doi.org/10.1680/geot.1970.20.4.387.

[101] Cerato AB, Lutenegger AJ. Scale effects of shallow foundation bearing capacity on granular material. Journal of Geotechnical and Geoenvironmental Engineering 2007;133(10):1192-1202. https://doi.org/10.1061/(ASCE)1090-0241(2007)133:10(1192).

Journal Pre-proofs

**List of Tables**

**Table 1** The soil properties used in the experiments.

**Table 2** Physical and mechanical properties of fabricated and scaled 3D-printed model geocells.

**Table 3** Experimental test program.

**Table 4** Comparison of improvement factors ($I_f$) for footings on geocell-reinforced sand at varying settlement ratios ($s/B$), as reported in various studies.

**Table 5** Material properties used for validating numerical models of geocell-reinforced systems: comparison of small-scale and prototype-scale (field condition).

**Table 6** Improvement factors for 3D-printed geocells and prototype numerical models at a settlement ($s$) of 10 mm.

Journal Pre-proofs

**Table 1** The soil properties used in the experiments.

| Description | Value | Reference |
|---|---|---|
| Unified Soil Classification System, *USCS* | SP | [62] |
| Specific gravity, $G_s$ | 2.63 | [63] |
| Average particle size, $D_{50}$ (mm) | 0.41 | [64] |

| | | |
|---|---|---|
| Coefficient of uniformity, $C_u$ | 1.57 | [64] |
| Coefficient of curvature, $C_c$ | 1.02 | [64] |
| Maximum void ratio, $e_{max}$ | 0.83 | [65] |
| Minimum void ratio, $e_{min}$ | 0.57 | [66] |
| Internal friction angle at $D_r$ of 75%, $\phi_{p75}$ (°) | 36 | [67] |
| Internal friction angle at $D_r$ of 35%, $\phi_{p35}$ (°) | 31 | [67] |
| Dilation angle at $D_r$ of 75%, $\psi$ (°) | 6 | [67] |

Journal Pre-proofs

**Table 2** Physical and mechanical properties of fabricated and scaled 3D-printed model geocells.

| Geocell type | Cell wall height (mm) | Pocket width ($b_g$) and length ($l_g$) (mm x mm) | Wall thickness (mm) | Secant tensile stiffness of geocell ($E_s$) at 2% strain (kN/m)** | Pattern |
|---|---|---|---|---|---|
| Fabricated (HDPE)* | 100 | 210 x 245 | 1.1 | 450 | Honeycomb |
| 3D-printed (scaled) | 33 | 70 x 82 | 0.6 | 50 | Rectangular |

*HDPE refers to high-density polyethylene.

** The secant tensile stiffness was determined according to ISO 527 [56].

Journal Pre-proofs

**Table 3** Experimental test program.

| Test series | Test type | Geocell | Constant parameters | Other parameters | | | | | No. of tests |
|---|---|---|---|---|---|---|---|---|---|
| | | | | *e/B* | $D_r$ (%) | $E_s$ at a strain of 2% (kN/m) | *h/B* | $b_g/B$ | |
| A | Unreinforced | - | - | | 35 | - | - | - | 2 |
| B | Unreinforced | - | - | | 75 | - | - | - | 2 |
| C | Reinforced | Fabricated | u/B=0.1, d/B=2.2, b/B=8 | 0, 1/6 | 35 | 450 | 1 | 2.1 | 2 |
| D | Reinforced | 3D-printed | | | 35 | 50 | 0.33 | 0.7 | 2 |
| E | Reinforced, | Fabricated | | | 75 | 450 | 1 | 2.1 | 2 |
| F | Reinforced | 3D-printed | | | 75 | 50 | 0.33 | 0.7 | 2 |

Journal Pre-proofs

**Table 4** Comparison of improvement factors ($I_f$) for footings on geocell-reinforced sand at varying settlement ratios ($s/B$), as reported in various studies.

| Reference | Test type | Footing type | Geocell type | $D_r$ (%) | ϕ (°) | B or D (m) | u/B or u/D | h/B or h/D | $b_g$/B or $b_g$/D | b/B or b/D | Secant tensile stiffness ($E_s$)-tensile strength (T) of geocell, (kN/m) | $I_f$ (s/B=3%) | $I_f$ (s/B=5%) | $I_f$ (s/B=10%) | $I_f$ (s/B=20%) |
|---|---|---|---|---|---|---|---|---|---|---|---|---|---|---|---|
| Dash et al. [22] | Small scale | Strip | Geogrid | 30 | 39.2 | 0.1 | 0.1 | 1.6 | 1.2 | 8 | 160[a]-20 | 1.48 | 1.56 | 1.90 | 2.55 |
| | | | | 50 | 41 | | | | | | | 1.60 | 1.74 | 2.12 | 3.00 |
| | | | | 70 | 42.2 | | | | | | | 1.68 | 1.83 | 2.29 | 4.24 |
| Dash et al. [22], Dash [37] | Small scale | Strip | Geogrid | 70 | 42.2 | 0.1 | 0.1 | 1.2 | 1.5 | 8 | 70[a]-4.5 | 1.03 | 1.10 | 1.52 | 2.71 |
| | | | | | | | | | | | 70[a]-7.5 | 1.25 | 1.30 | 1.74 | 3.03 |
| | | | | | | | | | | | 160[a]-20 | 1.13 | 1.24 | 1.76 | 3.12 |
| Sitharam and Sireesh [42] | Small scale | Circular | Geogrid | 70 | 41 | 0.15 | 0.05 | 1.8 | 0.8 | 4.9 | 160[a]-20 | 1.75 | 1.79 | 2.63 | 4.11 |
| Latha and Somwanshi [43] | Small scale | Square | Geogrid | 70 | 44 | 0.15 | 0.05 | 0.6 | 0.55 | 4.9 | 160[a]-20 | 1.18 | 1.30 | 1.93 | 3.36 |
| Dash [75] | Small scale | Strip | Geogrid | 30 | 39.2 | 0.1 | 0.1 | 1.6 | 1.2 | 8 | 160[a]-20 | 1.48 | 1.56 | 1.90 | 2.55 |
| | | | | 40 | | | | | | | | 1.54 | 1.72 | 2.08 | 2.90 |
| | | | | 50 | 41 | | | | | | | 1.60 | 1.74 | 2.12 | 3.00 |

Journal Pre-proofs

| | | | | | | | | | | | | | | | |
|---|---|---|---|---|---|---|---|---|---|---|---|---|---|---|---|
| | | | | 60 | | | | | | | | 1.64 | 1.81 | 2.26 | 3.80 |
| | | | | 70 | 42.2 | | | | | | | 1.68 | 1.83 | 2.29 | 4.24 |
| Moghaddas Tafreshi and Dawson [71] | Small scale | Strip | PP | 72 | 37.5 | 0.075 | 0.1 | 1.33 | 0.67 | 4.2 | NG-13.1 | 2.69 | 2.74 | 3.11 | NG |
| Gurbuz and Mertol [7] | Small scale | Strip | HDPE | 55 | 30 | 0.07 | 0.1 | 1.07 | 4.1 | 8.2 | NG | 2.05 | 2.14 | 2.33 | 3.12 |
| | | | | | | | | 2.14 | | | | 2.28 | 2.28 | 2.38 | 3.24 |
| Hegde and Sitharam [81] | Small scale | Square | PE | 65 | 30 | 0.15 | 0.1 | 1 | 1.67 | 5.9 | NG-21.5 | 1.25 | 1.3 | 1.5 | 1.9 |
| Moghaddas Tafreshi et al. [83] | Small scale | Circular | PP | 85 | 38.5 | 0.112 | 0.1 | 1.33 | 0.45 | 3.2 | NG-13.1 | 1.90 | 2.05 | 2.70 | 3.84 |
| Kargar and Hosseini [25] | Small scale | Strip | W. geotextile | 72 | NG | 0.05 | 0.1 | 1 | 1 | 5 | 72[a],275[c] -21.8 | 1.63 | 1.67 | 1.89 | NG |
| | | | | | | | | 1.5 | | | | 2.00 | 2.08 | 2.28 | NG |
| Sherin et al. [51] | Small scale | Square | PVC | 65 | 38 | 0.15 | 0.06 | 1.5 | 0.8 | 5 | 58.50-9.68 | NG | 4.58 | 3.39 | 3.34 |
| Simsek [78] | Small scale | Circular | HDPE | 64 | 37 | 0.26 | 0 | 0.77 | 1.34 | 3.84 | 5.61[a],7.79[c]-9.72 | 1.58 | 1.61 | 1.69 | 1.75 |

**Table 4** (Continued) Comparison of improvement factors ($I_f$) for footings on geocell-reinforced sand at varying settlement ratios ($s/B$) as reported in various studies.

Journal Pre-proofs

| Reference | Test type | Footing type | Geocell type | $D_r$ (%) | Φ (°) | B or D (m) | u/B or u/D | h/B or h/D | $b_g$/B or $b_g$/D | b/B or b/D | Secant stiffness ($E_s$)-tensile strength (T) of geocell, (kN/m) | $I_f$ (s/B=3%) | $I_f$ (s/B=5%) | $I_f$ (s/B=10%) | $I_f$ (s/B=20%) |
|---|---|---|---|---|---|---|---|---|---|---|---|---|---|---|---|
| Lal et al. [23] | Small scale | Square | Coir geotextile | 30 | NG | 0.15 | 0.1 | 0.5 | 0.33 | 3 | 94[b], 16[c] | 6.04 | 6.13 | 6.35 | 6.98 |
| | | | | 50 | | | | | | | | 6.11 | 6.23 | 6.59 | 7.09 |
| | | | | 60 | | | | | | | | 6.17 | 6.35 | 6.7 | 7.3 |
| | | | | 70 | | | | | | | | 6.25 | 6.41 | 6.9 | 7.52 |
| Kaur et al. [84] | Small scale | Strip | HDPE | 60 | 30 | 0.1 | 0.5 | 0.1 | NG | 6 | NG | NG | NG | NG | 3.5 |
| Kargar and Hosseini [85] | Small scale | Strip | W. geotextile | 72 | NG | 0.05 | 0.1 | 1.5 | 1 | 5 | 72[a], 275[c]-21.8 | 2.00 | 2.08 | 2.28 | NG |
| | | | Geogrid | | | | | | | | 110[c]-2.8 | 1.48 | 1.52 | 1.77 | NG |
| Shadmand et al.[18] | Large Scale | Square | NPA | 35 | 38 | 0.5 | 0.1 | 0.3 | 0.44 | 5 | NG-15 | 1.14 | 1.17 | 1.25 | 1.44 |
| | | | | 65 | 41 | | | | | | | 1.59 | 1.58 | 1.60 | NG |
| Li et al. [86] | Small Scale | Rectangular | PE | NG | 30 | 0.4 | 0.2 | 0.125 | 1 | 5 | 24 (MPa)-6.5 (MPa) | 3.38 | 2.57 | 2.08 | NG |
| Muthukumar et al. [87] | Small Scale | Square | Jute | 50 | 38 | 0.1 | 0.1 | 0.6 | 1 | 4 | NG-10.7 | 2.83 | 2.66 | 2.80 | 3.28 |

Journal Pre-proofs

| | | | | | | | | | | | | | | |
|---|---|---|---|---|---|---|---|---|---|---|---|---|---|---|
| Doley et al. [72,79] | Small scale | Square | W. geotextile | 70 | 40.5 | 0.15 | 0.1 | 0.66 | 0.5 | 5 | NG-24 | 2.01 | 2.34 | 2.80 | 3.73 |
| Fazeli Dehkordi et al. [53] | Large scale | Circular | HDPE | 40 | 31 | 0.4 | 0.1 | 0.38 | 0.46 | 4 | NG | 1.11 | 1.15 | 1.23 | 1.36 |
| | | | | 54 | 34 | | | | | | | 1.14 | 1.17 | 1.27 | 1.40 |
| | | | | 68 | 36 | | | | | | | 1.19 | 1.26 | 1.37 | 1.49 |
| | | | | 82 | 39 | | | | | | | 1.20 | 1.26 | 1.42 | 1.54 |
| Portakal [88] | Field condition | Square | HDPE | 70 | NG | 0.45 | 1.11 | 0.22 | 0.66 | 3.33 | NG-20 | 1.35 | NG | NG | NG |
| Jahanian et al. [73] | Small scale | Strip | Geogrid | 80 | NG | 0.1 | 0.1 | 0.6 | 0.57 | 4 | NG-3.03 | 1.53 | 1.57 | 1.58 | 2.00 |
| Sharma and Kumar [89] | Small scale | Ring | Geogrid | 80 | 36.3 | 0.3 | 0.1 | 1 | 0.35 | 6.5 | 280[a], 350[c]-20 | 2.55 | 2.57 | 2.81 | 3.20 |

Note: The acronyms *a*, *b* and *c* represent the secant stiffness of geocell material at 5% strain, failure and 2% strain, respectively. *NG* denotes that the information is not provided. The geotextile-based geocell materials are categorized as either woven (*W*) or non-woven (*N*). Generally, fabricated geocells are made of high-density polyethylene (HDPE) or novel polymeric alloy, known as Neoloy (*NPA*).

Journal Pre-proofs

**Table 5** Material properties used for validating numerical models of geocell-reinforced systems: comparison of small-scale and prototype-scale (field condition).

| | Small-scale (Laboratory test) | | Prototype-scale (Field condition) | |
|---|---|---|---|---|
| Parameters | Values | Values | Values | Values |
| **Sand** | Loose | Dense | Loose | Dense |
| Material model | Hardening Soil | Hardening Soil | Hardening Soil | Hardening Soil |
| Reference secant Young's modulus, $E_{50}^{ref}$ (kPa) | 3000 | 20000 | 9000 | 60000 |
| Refence tangent primary oedometer modulus, $E_{oed}^{ref}$ (kPa) | 3000 | 20000 | 9000 | 60000 |
| Reference un/reloading modulus, $E_{ur}^{ref}$ (kPa) | 9000 | 50000 | 27000 | 150000 |
| Internal friction angle, $\phi$ (◦) | 31 | 36 | 31 | 36 |
| Cohesion, $c$ (kPa) | 1 | 1 | 1 | 1 |
| Dilatancy angle, $\psi$ (◦) | 0 | 6 | 0 | 6 |
| Poisson ratio, $v$ | 0.2 | 0.3 | 0.2 | 0.3 |
| Unit weight, $\gamma$ (kN/m$^3$) | 14.8 | 15.8 | 14.8 | 15.8 |
| Exponential power, $m$ (-) | 0.5 | 0.5 | 0.5 | 0.5 |
| Failure ratio, $R_f$ (-) | 0.9 | 0.9 | 0.9 | 0.9 |
| Interface reduction factor, $R_{int}$ | 0.8 | 0.8 | 0.8 | 0.8 |
| **Geocell** | 3D-printed | Fabricated | 3D-printed | |
| Material model | Elastoplastic | | Elastoplastic | |

Journal Pre-proofs

| | | | |
|---|---|---|---|
| Pocket ($b_g$) width and length ($l_g$) (mm x mm) | 70 x 82 | 210 x 245 | 210 x 245 |
| Cell height (mm) | 33 | 100 | 100 |
| Thickness (mm) | 0.6 | 1.1 | 1.1 |
| Axial stiffness, *EA* (kN/m)* | 50 | 450 | 450 |
| **Footing** | | Steel plate | Steel plate |
| Material model | | Linear elastic | Linear elastic |
| Young's modulus, *E* (kPa) | | $2x10^9$ | $6x10^9$ |
| Poisson's ratio, *v* | | 0.25 | 0.25 |
| Unit weight, $\gamma$ (kN/m$^3$) | | 77 | 77 |
| Width, *B* (mm) | | 100 | 300 |
| Length, *L* (mm) | | 996 | 2988 |
| Thickness, *d* (mm) | | 20 | 60 |

* Axial stiffness (*EA*) values in PLAXIS 3D are equal to secant tensile stiffness of geocell materials in according to ISO 527 [56] at 2% strain.

**Table 6** Improvement factors for 3D-printed geocells and prototype numerical models at a settlement (*s*) of 10 mm.

| Scale | Reinforcement type | B (mm) | Geocell properties |
|---|---|---|---|

| | | | $D_r$ (%) | $E_s$ (kN/m) | h/B | $b_g$/B | $I_f$ |
|---|---|---|---|---|---|---|---|
| Small | Unreinforced | 100 | 35 | - | - | - | 1.8 |
| | Reinforced | 100 | | 50 | 0.33 | 0.7 | |
| Prototype (field condition) | Unreinforced | 300 | | - | - | - | 1.42 |
| | Reinforced | 300 | | 450 | 1 | 2.1 | |
| Small | Unreinforced | 100 | 75 | - | - | - | 1.26 |
| | Reinforced | 100 | | 50 | 0.33 | 0.7 | |
| Prototype (field condition) | Unreinforced | 300 | | - | - | - | 1.2 |
| | Reinforced | 300 | | 450 | 1 | 2.1 | |

Journal Pre-proofs

**List of Figures**

**Fig. 1.** Tensile stress vs. strain curves of dog-bone specimens for fabricated prototype and 3D-printed materials with 5% filling rate, along with a 1:9 scaled curve for the fabricated prototype.

**Fig. 2.** Tensile stress vs. strain curves of wide-width specimens for fabricated prototype and 3D-printed materials with 5% filling rate, along with a 1:9 scaled curve for the fabricated prototype.

**Fig. 3.** Fabrication of 1:3 scaled model geocells through 3D printing.

**Fig. 4.** Schematic representation of the experimental setup.

**Fig. 5.** Bearing pressure-settlement results obtained directly from the strip footings on unreinforced, 3D-printed and fabricated geocell-reinforced for: (a) loose sand ($D_r$=35%) and (b) dense sand ($D_r$=75%).

**Fig. 6.** Surface displacement profiles of 3D-printed and fabricated geocell reinforced strip footing under an eccentricity ratio of 1/6 in: (a) loose sand and (b) dense sand.

**Fig. 7.** Improvement factors obtained directly from laboratory tests for footings reinforced with fabricated or 3D-printed geocells under centric and eccentric loading of 1/6 in (a) loose and (b) dense sand.

**Fig. 8.** Approximate upper and lower boundaries of improvement factors against settlement ratios from small- and large-scale tests in existing literature, with data points from the present study.

**Fig. 9.** Numerical models of reinforced strip footings with (a) fabricated and (b) 3D-printed geocells under centric loading.

**Fig. 10.** Test results of small-scale laboratory tests verified with FE method for strip footings on (a) unreinforced and (b) 3D-printed and fabricated geocell reinforced sands under centric and eccentric loading of 1/6.

**Fig. 11.** Comparison of small-scale and prototype-scale numerical analyses with experimental test results of 3D-printed geocell-reinforced footing under centric loading.

**Fig. 12.** Distribution of incremental deviatoric strain for dense sand under centric loading (a) unreinforced small-scale, (b) 3D-printed geocell reinforced small-scale, (c) unreinforced prototype and (d) 3D-printed geocell reinforced prototype.

Journal Pre-proofs

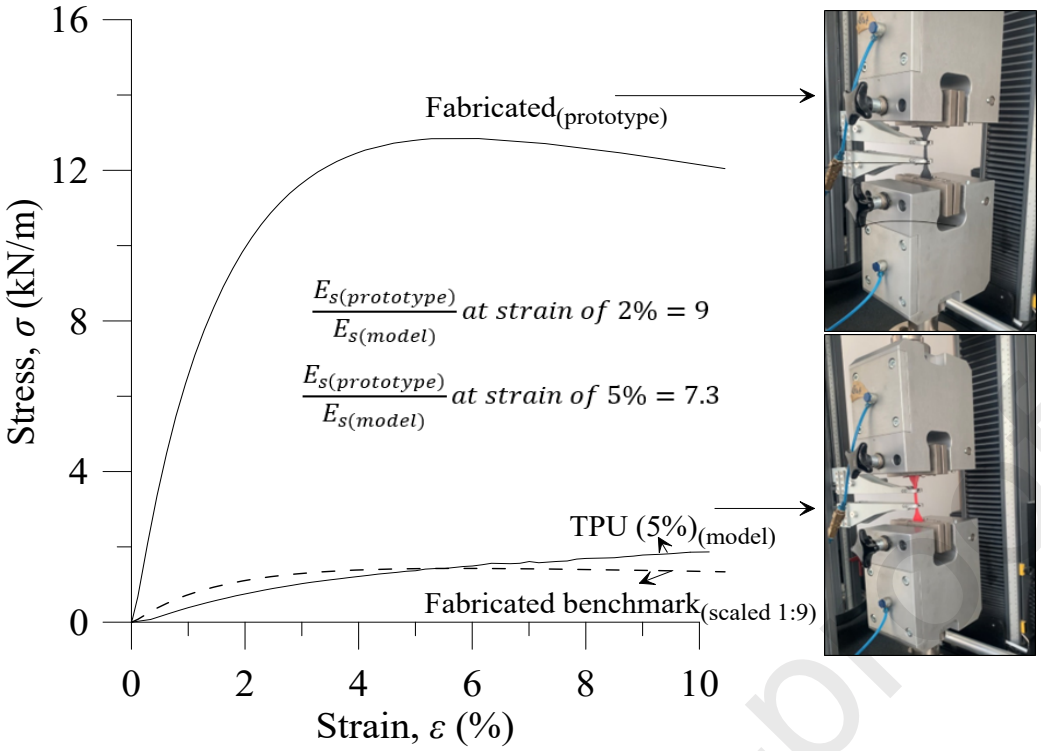


**Fig. 1.** Tensile stress vs. strain curves of dog-bone specimens for fabricated prototype and 3D-printed materials with 5% filling rate, along with a 1:9 scaled curve for the fabricated prototype.

Journal Pre-proofs

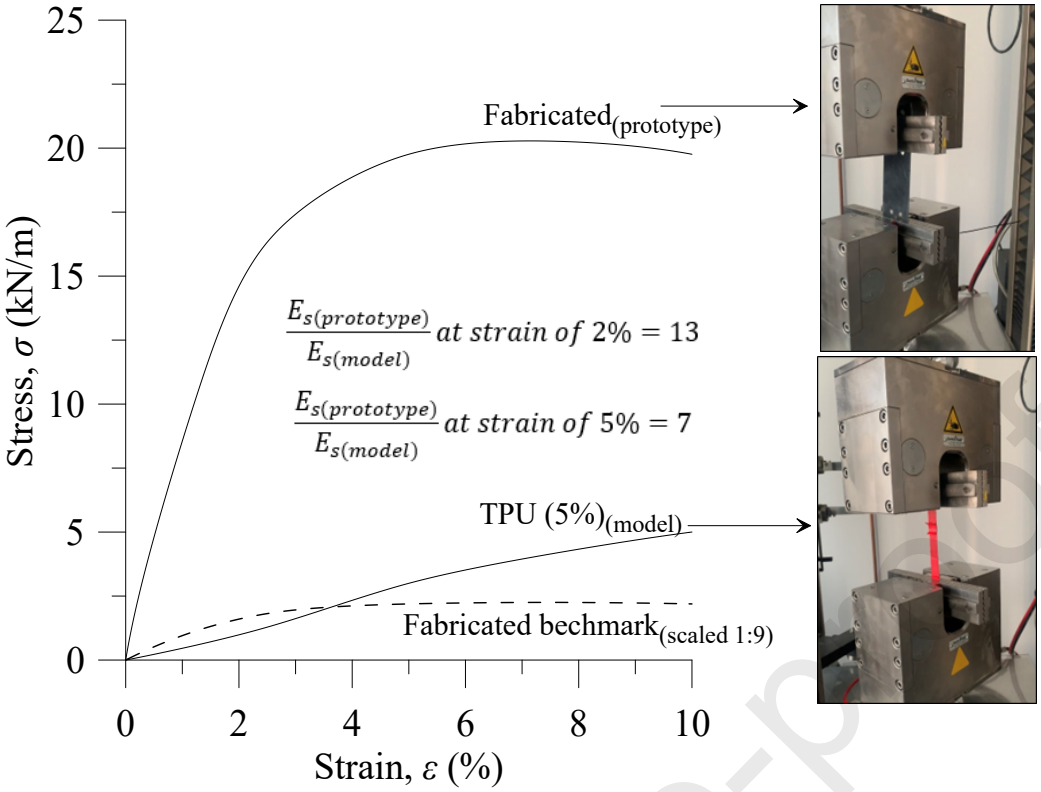


**Fig. 2.** Tensile stress vs. strain curves of wide-width specimens for fabricated prototype and 3D-printed materials with 5% filling rate, along with a 1:9 scaled curve for the fabricated prototype.

Journal Pre-proofs

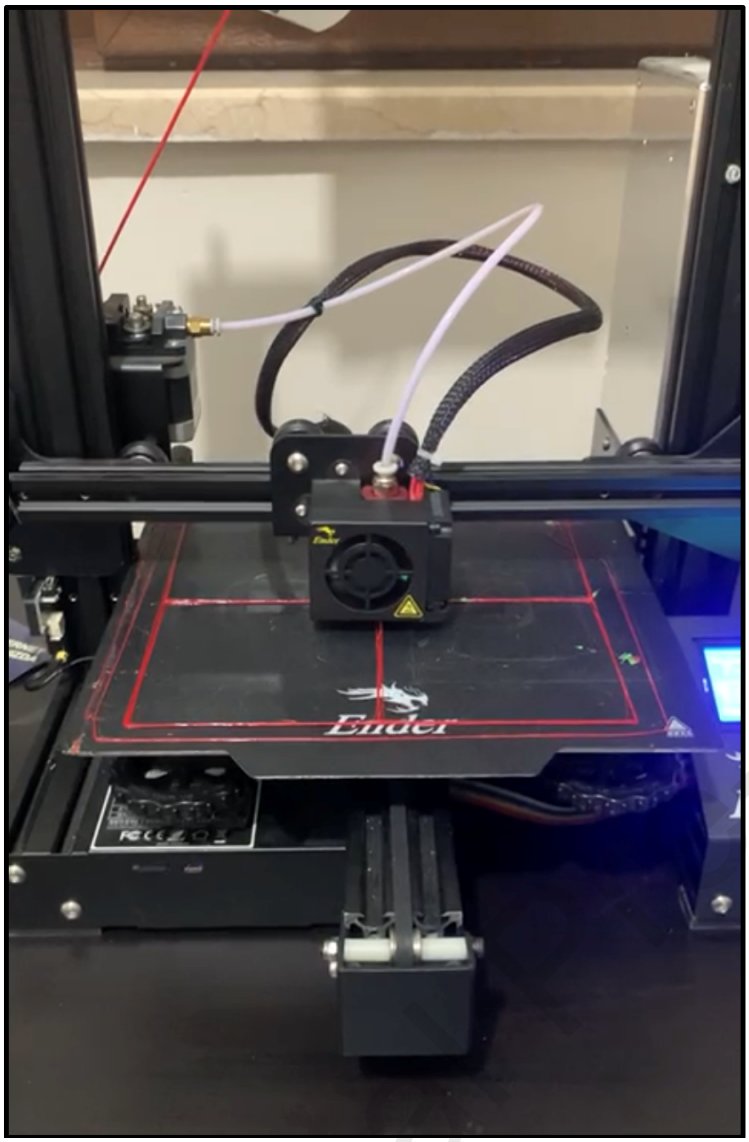


**Fig. 3.** Fabrication of 1:3 scaled model geocells through 3D printing.

Journal Pre-proofs

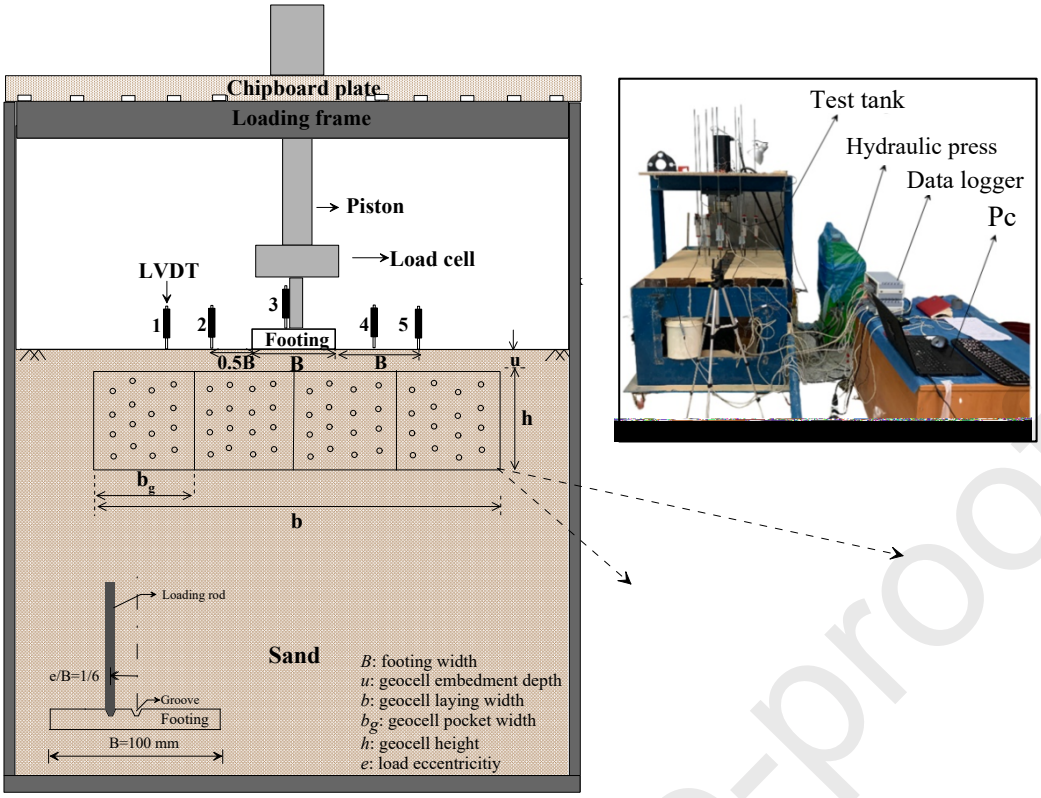


**Fig. 4.** Schematic representation of the experimental setup.

Journal Pre-proofs